Climate Dynamics (2020) 54:4485–4498
https://doi.org/10.1007/s00382-020-05239-w

# Effects of high-frequency surface wind on the intraseasonal SST associated with the Madden-Julian oscillation

Yingxia Gao[1,2] · Pang-Chi Hsu[1] · Lin Chen[1,3] · Lu Wang[1,3] · Tim Li[1,4]

Received: 15 April 2019 / Accepted: 9 April 2020 / Published online: 18 April 2020


## Abstract

The effect of high-frequency (< 20 days) wind on the intraseasonal sea surface temperature (SST) anomaly associated with the Madden-Julian oscillation (MJO) is examined by diagnosing reanalysis and outputs from a set of oceanic general circulation model (OGCM) experiments. Warm SST anomaly (SSTA) ahead of MJO convective center induces anomalous boundary-layer convergence, favoring the eastward propagation of the MJO. To understand the key physical processes contributing to the warm SSTA, the mixed-layer heat budget equation is diagnosed. The time change of SSTA ($\partial\langle T\rangle/\partial t$) mostly comes from shortwave radiative heating, while latent heat flux (LHF) plays the secondary role. Due to the strong nonlinearity of LHF, the high-frequency (< 20 days) wind may affect the intraseasonal LHF variability via interacting with the background state, resulting in changes in intraseasonal SSTA. Our diagnosis shows that the upscale feedback associated with high-frequency wind variability accounts for around 23% of the intraseasonal LHF in the intraseasonal SST warming region, supporting the growth of $\partial\langle T\rangle/\partial t$. Sensitivity experiments are then designed using an OGCM that simulates the upper-ocean temperature well, to verify the high-frequency wind effect on the intraseasonal SST variability. Once the high-frequency component of surface winds is removed in the model integration, the amplitudes of intraseasonal LHF and $\partial\langle T\rangle/\partial t$ are decreased, leading to reduced SSTA. The modeling results confirm the positive role of high-frequency wind in supporting the tropical intraseasonal SST variation. The findings of this study suggest that an accurate representation of high-frequency disturbances and their interaction with other components are crucial for MJO simulation and prediction.

**Keywords** Scale interaction · Air–sea interaction · Madden-Julian oscillation · High-frequency wind · Sea surface temperature

## 1 Introduction

Since the Madden-Julian oscillation (MJO; Madden and Julian 1971) was discovered, it has been a hot topic because of its significant modulations on weather and climate over the world (Zhang 2013). The MJO is characterized by planetary-scale activities at intraseasonal time scale (20–90 days), propagating eastward at ~ 5 m $s^{-1}$ along the equator (Madden 1986; Madden and Julian 1994; Zhang 2005). Active convection associated with the MJO appears over the warm pool region, while its related upper-level circulation anomalies travel around the world. Besides the atmospheric signals, intraseasonal signals have also been observed at and below the air–sea interface, such as sea surface temperature (SST), surface fluxes and mixed-layer depth (Krishnamurti et al. 1988; Zhang 1996; Lau and Sui 1997).

With abundant in situ measurements and reanalysis datasets, interaction between the atmosphere and ocean

✉ Pang-Chi Hsu
pangchi@nuist.edu.cn

1 Key Laboratory of Meteorological Disaster of Ministry of Education/Collaborative Innovation Center on Forecast and Evaluation of Meteorological Disasters/NUIST-UoR International Research Institute, Nanjing University of Information Science and Technology, Nanjing, China

2 School of Ecology and Environment, Inner Mongolia University, Hohhot, China

3 LASG, Institute of Atmospheric Physics (IAP), Chinese Academy of Sciences (CAS), Beijing, China

4 International Pacific Research Center, University of Hawaii at Manoa, Hawaii, USA

related to the MJO has been well studied (Lau and Waliser 2012; DeMott et al. 2015). Using the observational data from the international Cooperative Indian Ocean Experiment on Intraseasonal Variability in the Year 2011/Dynamics of the MJO (CINDY2011/DYNAMO) field campaign (Yoneyama et al. 2013), de Szoeke et al. (2015) found that the net surface heat flux into the ocean is ahead of the MJO event, warming the ocean. When the MJO convection is active, reduced shortwave radiative heating combined with enhanced evaporation appears at and to the west of the convective center, cooling the ocean (Gao et al. 2016). As a result, warm (cold) SST leads (lags) anomalous rainfall. This indicates that the ocean plays a passive role in the air–sea interaction at the intraseasonal time scale, largely forced by atmospheric convection. The ocean feedback to the intraseasonal convection has also been gradually identified (Waliser and Graham 1993; Woolnough et al. 2000; Klingaman and Woolnough 2014; DeMott et al. 2016). Hsu and Li (2012) diagnosed the role of SST anomaly (SSTA) in the eastward propagation of the MJO. They found that the SSTA gradient induces 10–25% of the boundary-layer convergence ahead of the MJO convective center, promoting the MJO propagation. DeMott et al. (2016) revealed that SST fluctuation supports the MJO convection along the equator, but damps off-equatorial convection. The intraseasonal SST also favors the eastward propagation of MJO over the MJO convective region through increasing both latent and sensible heat fluxes (LHF and SHF).

Surface moisture, heat and momentum play important roles in bridging the atmosphere and ocean (Hendon and Glick 1997; McPhaden 2002). As revealed by previous studies, intense multi-scale interaction exists in these surface variables (Zhou and Li 2010; Wang et al. 2015; Gao et al. 2019). Krishnamurti et al. (2003) calculated triple-product nonlinearities of surface heat fluxes in a frequency domain, and found that a great proportion of intraseasonal surface fluxes comes from the contribution of the MJO interacting with synoptic-scale activities. Based on two reanalysis datasets and several atmospheric general circulation model (AGCM) experiments, Gao et al. (2019) showed that high-frequency (< 20 days) disturbances can contribute 15–50% of the intraseasonal LHF variability through the interaction with the background state. Once the high-frequency components of surface variables associated with the LHF (wind and moisture) are removed, the simulated MJO convection is weakened and shows slower-moving activities compared to that in the simulation containing all time-scale components. Further diagnosis showed that this upscale feedback is largely attributed to the nonlinearity of low-level wind, as surface wind speed derived from the high-frequency zonal and meridional winds exhibits significant intraseasonal signals (Zhou and Li 2010).

Besides the upscale feedback of high-frequency wind to the MJO convection, Wang et al. (2015) found that high-frequency wind can explain about 20% of the boreal-summer intraseasonal SSTA variability over the mid-latitude North Pacific. The equatorial MJO with enhanced activity during the boreal winter also displays obvious air–sea interaction. Considering that the mean state and high-frequency variability over the equatorial area may show different features as those observed in the mid-latitude, our study here aims to understand how and to what extent the high-frequency winds can affect the intraseasonal SSTA associated with the MJO in the equatorial region. This paper is organized as follows. Data, analysis methods and numerical experiments are introduced in Sect. 2. In Sect. 3, we present the importance of SST variability in MJO convection and possible influence of high-frequency surface winds on intraseasonal SSTA variability. By using a set of oceanic general circulation model (OGCM) experiments, the high-frequency wind effect on intraseasonal SSTA is verified in Sect. 4. Summary and discussion are given in Sect. 5.

## 2 Data, methods and numerical experiments

### 2.1 Data

The following reanalysis datasets are used in this study: (1) daily outgoing longwave radiation (OLR) from the National Oceanic and Atmospheric Administration (NOAA) (Liebmann and Smith 1996) at a resolution of $2.5° \times 2.5°$ for 1979–2013; (2) daily surface data from the Modern-Era Retrospective Analysis for Research and Applications (MERRA; Rienecker et al. 2011) at a resolution of $0.5° \times 2/3°$ for 1979–2015; and (3) pentad ocean data from the National Centers for Environmental Prediction (NCEP) Global Ocean Data Assimilation System (GODAS; Behringer and Xue 2004) at a resolution of $0.5° \times 1°$ for 1980–2015. Surface variables from the MERRA include SST, surface shortwave (SW) and longwave (LW) radiative heating, surface latent and sensible heat fluxes (LHF and SHF), and the variables needed to compute LHF. For the mixed-layer heat budget analysis, oceanic variables from the GODAS include mixed-layer depth, three-dimensional temperature, zonal, meridional and vertical current velocities. Before analysis, the pentad GODAS data are interpolated to daily values. In the OGCM experiments, daily surface data from the MERRA for 1979–2015 are employed as the forcing fields. In this study, the MJO is defined as the 20–90-day-filtered variability during the boreal winter (December–February, or DJF).

## 2.2 Budget analysis

### 2.2.1 Boundary-layer momentum budget

SSTA and its gradient can induce hydrostatic effect on boundary-layer pressure, and cause boundary-layer convergence (Lindzen and Nigam 1987). By using long-time fine-resolution reanalysis datasets, we examine the importance of the ocean in atmospheric convection during different MJO phases based on this mechanism. The boundary-layer momentum equation developed by Wang and Li (1993) is adopted here:

$$f\boldsymbol{k}\times\boldsymbol{V}_B^{'}+E\boldsymbol{V}_B^{'}=-\nabla\emptyset_e^{'}+\frac{R\cdot\left(P_s-P_e\right)}{2P_e}\cdot\nabla T_s^{'} \tag{1}$$

where the prime denotes the intraseasonal (20–90 days) component; $f$ is the Coriolis parameter; $\boldsymbol{k}$ is the unit vector in the vertical direction; $\boldsymbol{V}_B$ is the vertically averaged horizontal wind in the boundary layer; $E$ is the friction coefficient ($10^{-5}$ $s^{-1}$); $\nabla$ is the horizontal gradient operator; $\emptyset_e$ is the geopotential at the top of the boundary layer; $R$ is the gas constant of air; $P_s$ and $P_e$ are the pressures at the bottom and top of the boundary layer, respectively; and $T_s$ is surface temperature. The two terms on the right-hand side of Eq. (1) denote the effects on the boundary-layer convergence from the free-atmospheric wave and SSTA forcing, respectively. We will focus on the latter. The planetary boundary-layer thickness used in this study is 1000–850 hPa.

### 2.2.2 Mixed-layer heat budget

To quantitatively investigate the contribution of a specific process to the time change of SSTA, intraseasonal SSTA is analyzed through the mixed-layer heat budget equation. Following Li et al. (2002), we have:

$$\begin{aligned}\frac{\partial\langle T'\rangle}{\partial t}=&\left(\frac{LHF}{\rho C_pH}\right)^{'}+\left(\frac{SHF}{\rho C_pH}\right)^{'}+\left(\frac{SW}{\rho C_pH}\right)^{'}+\left(\frac{LW}{\rho C_pH}\right)^{'}\\&-\left\langle u\cdot\frac{\partial T}{\partial x}\right\rangle^{'}-\left\langle v\cdot\frac{\partial T}{\partial y}\right\rangle^{'}-\left\langle\omega\cdot\frac{\partial T}{\partial z}\right\rangle^{'}\end{aligned} \tag{2}$$

where $T$ is ocean temperature; $\rho$ is seawater density; $C_p$ is the specific heat of sea water; $H$ is mixed-layer depth; $u$, $v$ and $\omega$ are ocean zonal, meridional and vertical current velocities, respectively. The first four terms on the right-hand side of Eq. (2) denote the contributions from surface heat fluxes to temperature tendency ($\partial\langle T\rangle/\partial t$), and the last three terms are associated with ocean dynamic processes. Angled brackets represent the vertical average from the ocean surface to the bottom of the mixed layer, namely, the mixed-layer depth, defined as the depth at which ocean temperature is 0.8 °C colder than the SST.

As the mixed-layer depth over the warm pool region is shallow (~ 30 m) (de Boyer Montégut 2004; Drushka et al. 2012), SW may penetrate below the mixed layer. Following Duvel et al. (2004), we write SW absorbed in the mixed layer as follows:

$$SW=SW_{surf}-\left(0.58\times e^{-H/0.31}+0.42\times e^{-H/20}\right)*SW_{surf} \tag{3}$$

where $SW_{surf}$ is surface shortwave radiative heating.

### 2.2.3 Surface heat flux bulk formula

High-frequency wind may impact intraseasonal SSTA via surface LHF and SHF. As the amplitude of SHF is about an order smaller than that of LHF (DeMott et al. 2016), only LHF is considered when calculating the upscale feedback of high-frequency wind to the intraseasonal SSTA. The LHF bulk formula (Weare et al. 1981) is adopted as follows:

$$LHF=\rho L_vC_e\sqrt{u^2+v^2}\Delta q \tag{4}$$

where $\rho$ here is the near-surface air density; $L_v$ is the latent heat of condensation; $u$ and $v$ are the zonal and meridional winds at 10 m above the surface, respectively. $\Delta q$ is the specific humidity difference between the sea surface and near-surface atmosphere (10 m above the surface). $C_e$ is the constant transfer coefficient for moisture. It is set to $0.9\times10^{-3}$, simply determined by dividing the boreal winter mean LHF of the MERRA by the calculated LHF based on the bulk formula without including $C_e$.

To obtain the intraseasonal LHF nonlinearly rectified by the high-frequency wind, we use the method in Gao et al. (2019). All variables used to calculate LHF ($u$, $v$ and $\Delta q$) are first decomposed into three parts: the low-frequency background state (> 90 days), intraseasonal component (20–90 days) and high-frequency disturbances (< 20 days). Based on the bulk formula, LHF is computed by using the sum of low-frequency and high-frequency components of individual fields without the inclusion of intraseasonal time scale. The derived LHF is then subjected to 20–90-day band-pass filtering. This intraseasonal LHF comes from the high-frequency disturbances interacting with the low-frequency background state (referred to as "HF–LFBS interaction"). As revealed by Gao et al. (2019; their Fig. 8), the HF–LFBS interaction induced intraseasonal LHF is mostly contributed by the high-frequency wind interacting with background moisture state. We also compared the nonlinearly rectified LHF derived from "HF–LFBS interaction" method with that contributed by the high-frequency wind interacting with full time-scale $\Delta q$, and results were highly similar (not shown). We adopt the same method of "HF–LFBS interaction" in Gao et al. (2019) to carry out some discussions regarding their study.

### 2.3 Phase composite

In our reanalysis diagnosis, the phases of the MJO are determined by the Real-time Multivariate MJO (RMM) indices developed by Wheeler and Hendon (2004). The RMM indices are calculated by using the multiple-variable empirical orthogonal function (EOF) of daily OLR, 850- and 200-hPa zonal wind anomalies. They partition the life cycle of the MJO to eight phases (phases 1–8). For composite analysis, only the days with significant MJO signals (i.e., RMM amplitude $\geq 1.0$) are selected.

Since the OGCM does not produce the fields for deriving the RMM indices, an SSTA index is adopted to define the life cycle of intraseasonal SSTA as in Wang et al. (2012). It is based on the time series of the intraseasonal SSTA averaged over a reference region, and divides the local SSTA oscillation into 12 phases ($-180°$ to $0°$ to $180°$) with an interval of 30°. The point at which the SSTA reaches the maximum (minimum) is set as phase $0°$ ($-180°/180°$). Similarly, for phase composite, only the SSTA oscillations with amplitude exceeding one standard deviation are included.

### 2.4 Numerical experiments

To examine the influence of high-frequency wind on the intraseasonal SSTA variability, we adopt LICOM2.0, the OGCM developed by the Institute of Atmospheric Physics of the Chinese Academy of Sciences (IAP/CAS), version 2.0 (Liu et al. 2012). LICOM2.0 is also the ocean component of the Flexible Global Ocean–Atmosphere–Land System model (FGOALS-s2; Lin et al. 2013), which participated in the Coupled Model Intercomparison Project phase 5 (CMIP5; Ahn et al. 2017). It has a resolution of $1° \times 1°$ and 30 levels with the interval of the top 15 levels being 10 m thick. Compared to its previous version (LICOM1.0; Jin et al. 1999), which was used to investigate the El Nino–Southern Oscillation (ENSO), the Indian Ocean dipole mode as well as the intraseasonal oscillation (Yu and Sun 2009; Yuan and Liu 2009; Wang et al. 2015), LICOM2.0 includes some new parameterization schemes (such as the updated vertical mixing scheme and solar radiation penetration scheme), in addition to increased horizontal and vertical resolutions (Canuto et al. 2001, 2002; Ohlmann 2003). The bulk formula of Large and Yeager (2004) is chosen as the thermal forcing scheme for LICOM2.0. Thus, all the variables used to compute the surface LHF, SHF and wind stress are the forcing fields for the numerical experiments, such as surface wind, temperature and specific humidity. Through retaining or removing the high-frequency component of wind fields in model integration, we may understand the impact of high-frequency winds on the intraseasonal SSTA.

Two experiments are designed to evaluate oceanic responses to the high-frequency wind: a control run (CTRL) and a sensitivity experiment (EXP_noHF). In CTRL, the forcing fields contain all time scales (i.e., the sum of low-frequency, intraseasonal and high-frequency components), while in EXP_noHF, the high-frequency components of surface zonal and meridional winds are removed. Each experiment is integrated for 29 years. The differences between the intraseasonal SSTAs simulated by CTRL and EXP_noHF should reflect the importance of high-frequency wind to the intraseasonal SSTA variability.

## 3 Reanalysis data diagnosis

### 3.1 Role of SSTA in MJO dynamics

Figure 1 illustrates the distributions of boreal-winter (DJF) mean and standard deviation of SST, and of standard deviation of 20–90-day-filtered SSTA. Warm SST is observed from the Indian Ocean to the central Pacific, with amplitude exceeding 28 °C (Fig. 1a). In contrast, the standard deviation of SST (Fig. 1b) shows small values over the warm pool region, and maxima over the central-eastern equatorial Pacific where the interannual variability (such as the ENSO) is energetic (Zhang and Gottschalck 2002). On the intraseasonal time scale, vigorous SSTA variability is observed in the Southern Hemisphere during the boreal winter (Fig. 1c). Larger values appear in the Indian Ocean than in the western Pacific, which is the consequence of shallower mixed-layer depth in the Indian Ocean than in the western Pacific (Duvel and Vialard 2007). To clearly reveal the SST variability explained by the intraseasonal component, we calculate the ratio of the standard deviation of intraseasonal SSTA (Fig. 1c) to that of (total) SST (Fig. 1b) in Fig. 1d. The ratio shows large values in the equatorial Indian Ocean, Maritime Continent and western Pacific south of the equator. It is generally consistent with the distribution of active MJO regions. In these regions, (total) SST variability is significantly modulated by the intraseasonal SSTA, as more than 50% of the (total) SST variability comes from the intraseasonal component. The maximum ratio is observed in the eastern Indian Ocean and Maritime Continent (90°–150° E, 15° S–0°), where the intraseasonal SSTA is also quite strong. Thus, this region is selected as the key region for our reanalysis diagnosis.

Based on the RMM indices, we show the evolutions of MJO convection and SSTA (Fig. 2). The MJO convection exhibits pronounced eastward propagation from the Indian Ocean to the western Pacific (from phase 1 to phase 8). The intraseasonal SSTA also moves eastward but does not propagate as far into the western Pacific as the MJO convection. It shows most large values over the key region, with maxima in phases 2–3 and minima in phases 6–7. It is obvious that warm (cold) SSTA always leads (lags) the MJO convective

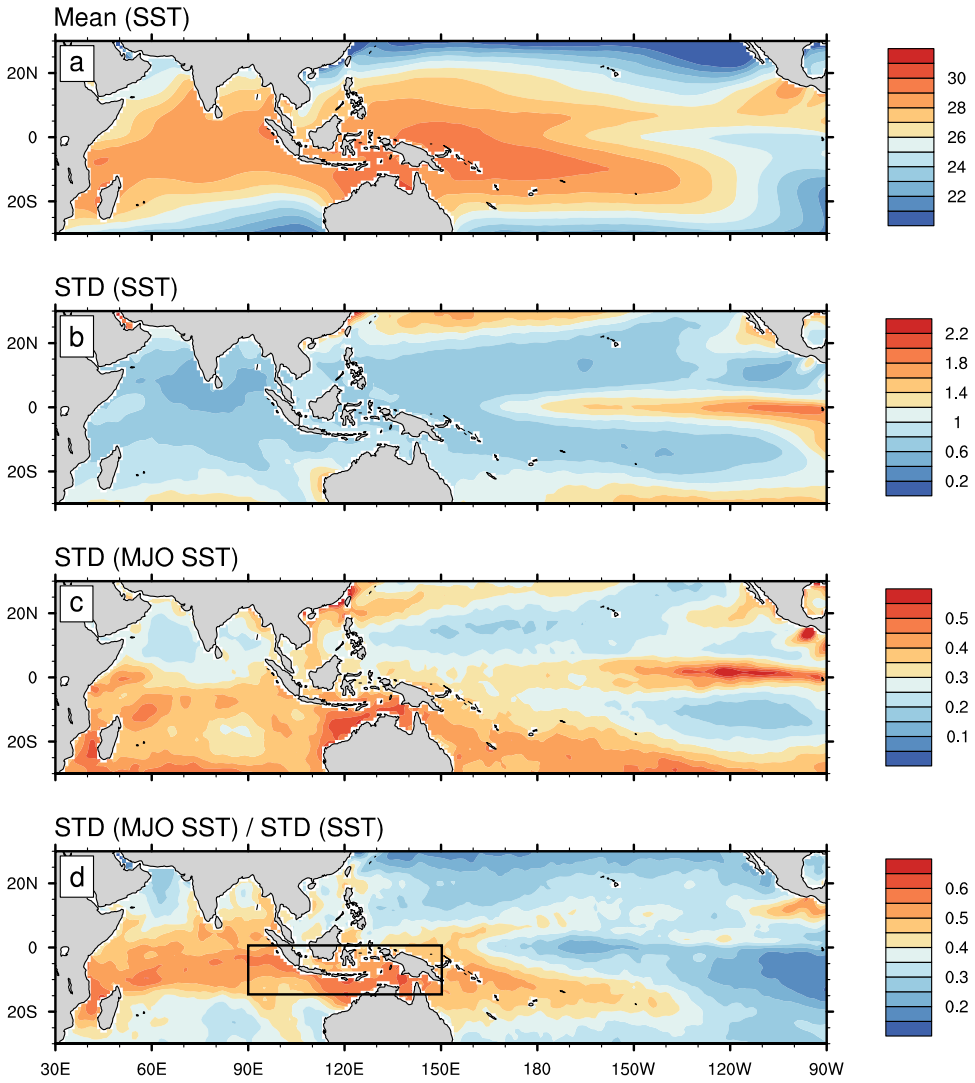


**Fig. 1** **a** Climatological mean and **b** standard deviation of SST. **c** Standard deviation of 20–90-day-filtered SSTA. Units: K. **d** The ratio of the standard deviation shown in **c** vs. that in **b**. The box in **d** represents the key region (90°–150° E, 15° S–0°) used for reanalysis diagnosis

center (Woolnough et al. 2000). Based on coarse-resolution SST data, Hsu and Li (2012) suggested that this gradient of SSTA is conductive to the eastward propagation of the MJO by modifying the boundary-layer stability. Our study aims to examine the role of intraseasonal SSTA in MJO dynamics based on this mechanism, but we use long-term fine-resolution reanalysis data. Figure 3 shows the 15° S–0° averaged intraseasonal OLR, SSTA and SSTA-forced boundary-layer divergence anomalies in phases 2–3 and 6–7, respectively. When the intraseasonal SSTA presents large values in the eastern Indian Ocean and Maritime Continent in phases 2–3, the MJO convection is located over the central Indian Ocean. The warm SSTA shows ~ 90° ahead of the convective center. In the warm SSTA region, there is anomalous SSTA-forced boundary-layer convergence. This confirms that positive intraseasonal SSTA gradient can induce boundary-layer convergence, which increases the atmospheric instability ahead of the convective center and contributes to the eastward propagation of the MJO. The intraseasonal variables in phases 6–7 exhibit near-mirror images with those in phases 2–3, with negative SSTA ~ 90° ahead of the suppressed MJO convection. Negative SSTA gradient induces anomalous boundary-layer divergence, conductive to the suppressed convection of MJO eastward propagation as well.

A number of studies pointed out that the oceanic fluctuation is strongly forced by the atmospheric convection via surface heat fluxes (Hendon and Glick 1997; Lau and Sui 1997; Duvel and Vialard 2007). What are the quantitative contributions of each surface heat flux term to the time change of SSTA? Figure 4a–b show the lead-lag relationships between the intraseasonal SSTA and its tendency (dSSTA/dt) averaged over the key region during phases 2–3 and 6–7, respectively. Intense warming (cooling) appears about 1 week before the intraseasonal SSTA maximum (minimum). More broadly, dSSTA/dt shows large values from lags − 20 to − 3 days. Thus, we define lags − 20 to − 3 days as the warming and cooling periods of the intraseasonal SSTA. To assess the contribution of each heating

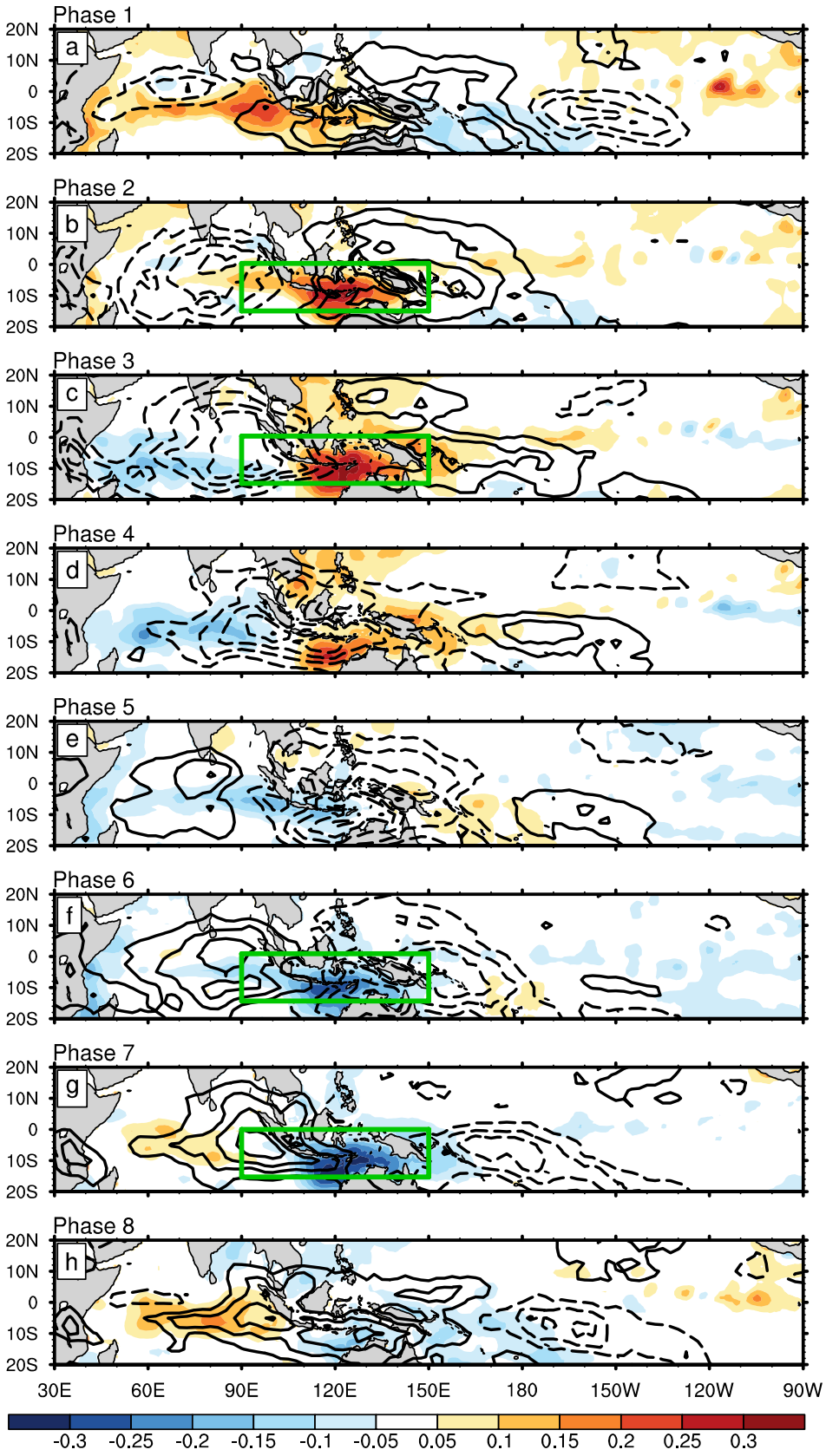


**Fig. 2** RMM phase evolutions of 20–90-day-filtered OLR (contour; W $m^{-2}$) and SSTA (shading; K). The outer-most solid (dashed) contour starts from 5 (−5) W $m^{-2}$, and the contour interval is 5 W $m^{-2}$. Green box represents the key region (90°–150° E, 15° S–0°)

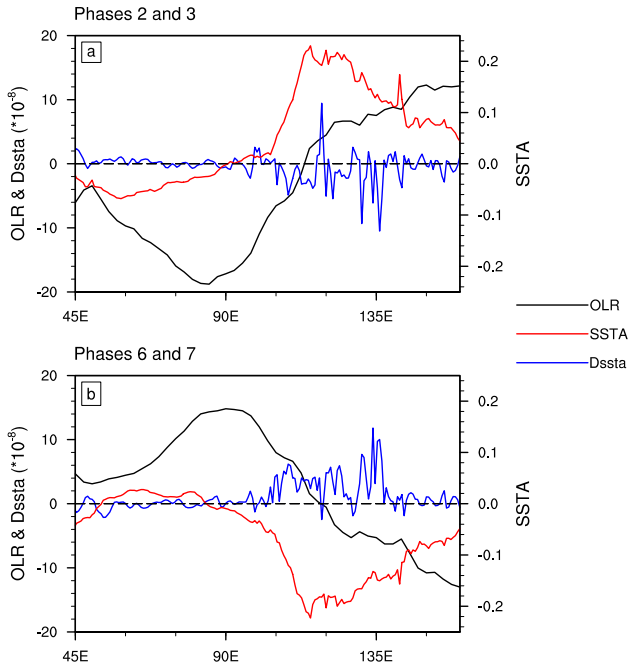


**Fig. 3** Phase relationships among 20–90-day-filtered OLR (black; W $m^{-2}$ on the left *y*-axis), SSTA-induced low-level divergence (Dssta; blue; $10^{-8}$ $s^{-1}$ on the left *y*-axis) and SSTA (red; K on the right *y*-axis), averaged over 15° S–0° in **a** phases 2 and 3 and **b** phases 6 and 7, when the intraseasonal SSTA shows its maxima and minima, respectively

process to the time change of SSTA, the mixed-layer heat budget equation (Eq. 2) is diagnosed. As shown in Fig. 4c, d, the sum of all temperature tendency terms is approximately equal to $\partial\langle T'\rangle/\partial t$ in both warming and cooling periods, despite of some underestimates. The residual suggests that some processes may be underestimated or overestimated. As expected, SW is the largest contributor to $\partial\langle T'\rangle/\partial t$, due to the abundant solar energy over the tropics. SSTA warming is decreased by LW, which is also controlled by convective clouds. MJO convection is nearly out of phase with $\partial\langle T'\rangle/\partial t$ as a result of in-quadrature phase relationship between SSTA and convection (Fig. 3), as well as between $\partial\langle T'\rangle/\partial t$ and SSTA (Fig. 4a, b). The second contributor is LHF, which accounts for about 13.4% of the intraseasonal $\partial\langle T\rangle/\partial t$. The contribution from SHF is nearly zero. The advection of temperature also favors $\partial\langle T'\rangle/\partial t$, but with small amplitude. This may be explained by the relatively uniform distribution of temperature over the warm pool region (Fig. 1a). Similar roles of these processes in $\partial\langle T'\rangle/\partial t$ occur during the cooling period (Fig. 4d). $\partial\langle T'\rangle/\partial t$ is mostly supported by SW and LHF, and decreased by LW. Surface heat fluxes play essential roles in the time change of SSTA.

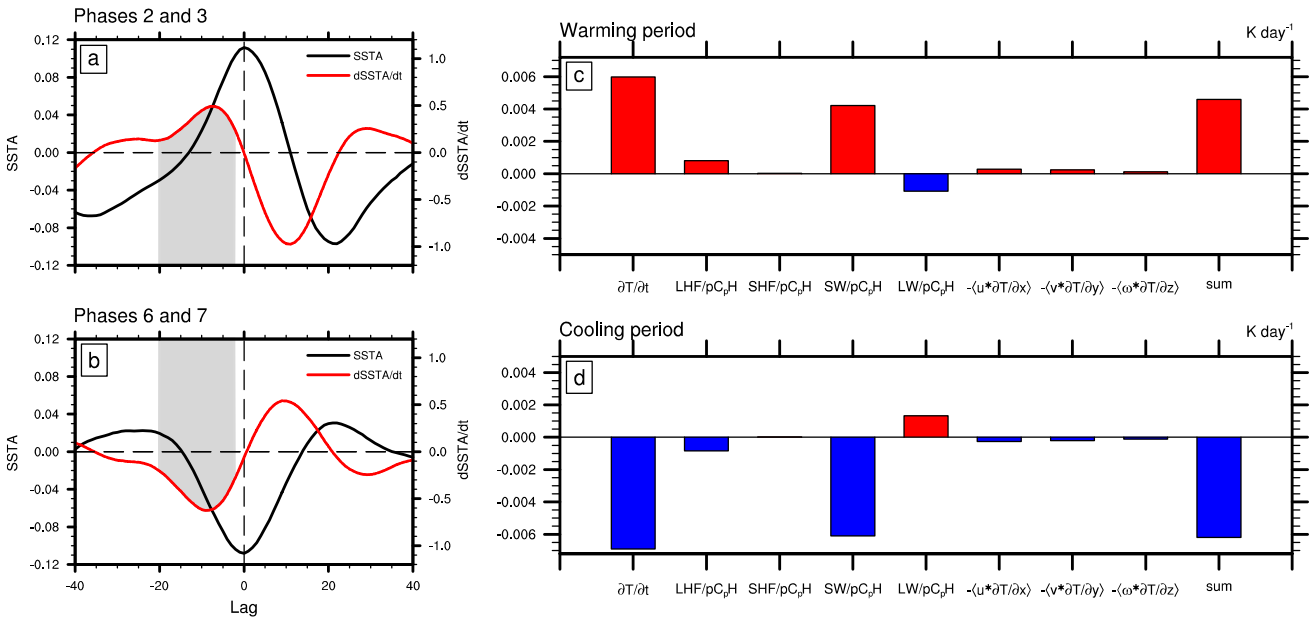


**Fig. 4** Lead-lag relationship between 20–90-day-filtered SSTA (black; K on the left *y*-axis) and its tendency (dSSTA/dt; red; K $day^{-1}$ on the right *y*-axis), averaged over (90°–150° E, 15° S–0°) in **a** phases 2 and 3 and **b** phases 6 and 7. Grey area in **a** and **b** indicates the warming and cooling periods, respectively. **c**, **d** Composites of individual intraseasonal SSTA tendency terms (K $day^{-1}$), averaged over (90°–150° E, 15° S–0°), for the **c** warming and **d** cooling periods, respectively. The bars are mixed-layer-averaged $\partial\langle T\rangle/\partial t$, $\mathrm{LHF}/\rho C_p H$, $\mathrm{SHF}/\rho C_p H$, $\mathrm{SW}/\rho C_p H$, $\mathrm{LW}/\rho C_p H$, $-\langle u\cdot\partial T/\partial x\rangle$, $-\langle v\cdot\partial T/\partial y\rangle$, $-\langle\omega\cdot\partial T/\partial z\rangle$, and the sum of all budget terms on the right-hand side of Eq. (2)

### 3.2 Effects of high-frequency wind on the intraseasonal SSTA

As shown in the mixed-layer heat budget analysis (Fig. 4), LHF plays a non-negligible role in the oceanic response to the intraseasonal convection. Previous studies revealed that significant nonlinear interaction between high-frequency disturbances and intraseasonal oscillation exists in LHF (Zhou and Li 2010; Gao et al. 2019). In this subsection, we aim to examine the effect of high-frequency wind on the intraseasonal SSTA through the rectification of LHF and $\partial\langle T\rangle/\partial t$.

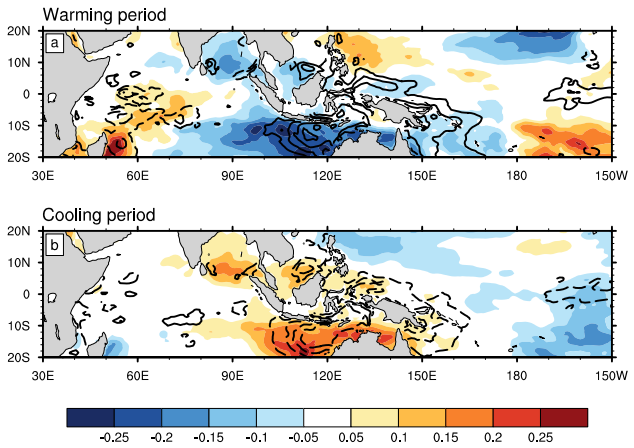


**Fig. 5** Composites of 20–90-day-filtered $\partial\langle T\rangle/\partial t$ (contour; K day$^{-1}$) and high-frequency (< 20-day) wind speed (shading; m s$^{-1}$) for the **a** warming and **b** cooling periods. The outer-most solid (dashed) contour starts from 0.003 (−0.003) K day$^{-1}$, and the contour interval is 0.003 K day$^{-1}$

Figure 5 illustrates the composites of intraseasonal $\partial\langle T\rangle/\partial t$ and high-frequency wind speed during the warming and cooling periods, respectively. The high-frequency wind speed anomaly is derived from the < 20-day zonal and meridional winds. Note that there is weaker (stronger) high-frequency wind over the positive (negative) $\partial\langle T'\rangle/\partial t$ region. On one hand, it suggests that the distribution of high-frequency wind is largely determined by MJO-related activities (Zhou and Li 2010). Active MJO convection, which generally coincides with negative $\partial\langle T'\rangle/\partial t$, provides a favorable environment for high-frequency wind. On the other hand, this high-frequency wind may exert an upscale impact on intraseasonal $\partial\langle T\rangle/\partial t$ by modifying LHF anomaly. As revealed by Gao et al. (2019), 15–50% of the intraseasonal LHF comes from high-frequency disturbances interacting with the background state across the warm pool.

Figure 6 shows the patterns of intraseasonal LHF calculated based on the total fields and HF–LFBS interaction without MJO contributions (described in Sect. 2.2c). The total intraseasonal LHF is located slightly to the west of maximum $\partial\langle T'\rangle/\partial t$, showing negative (positive) values over the positive (negative) $\partial\langle T'\rangle/\partial t$ region (Fig. 6a, c). This gives an explanation for the positive contribution of intraseasonal LHF to $\partial\langle T'\rangle/\partial t$ (Fig. 4c, d). The distribution of HF–LFBS interaction induced intraseasonal LHF (Fig. 6b, d) is highly similar to that of high-frequency wind (Fig. 5) and to that of the total intraseasonal LHF (Fig. 6a, c). Reduced (enhanced) LHF anomaly appears over the weak (strong) high-frequency wind region. Like the total intraseasonal LHF, the nonlinearly rectified LHF also contributes to $\partial\langle T'\rangle/\partial t$. The contribution from HF–LFBS interaction induced intraseasonal LHF to $\partial\langle T'\rangle/\partial t$ accounts for 22.6%

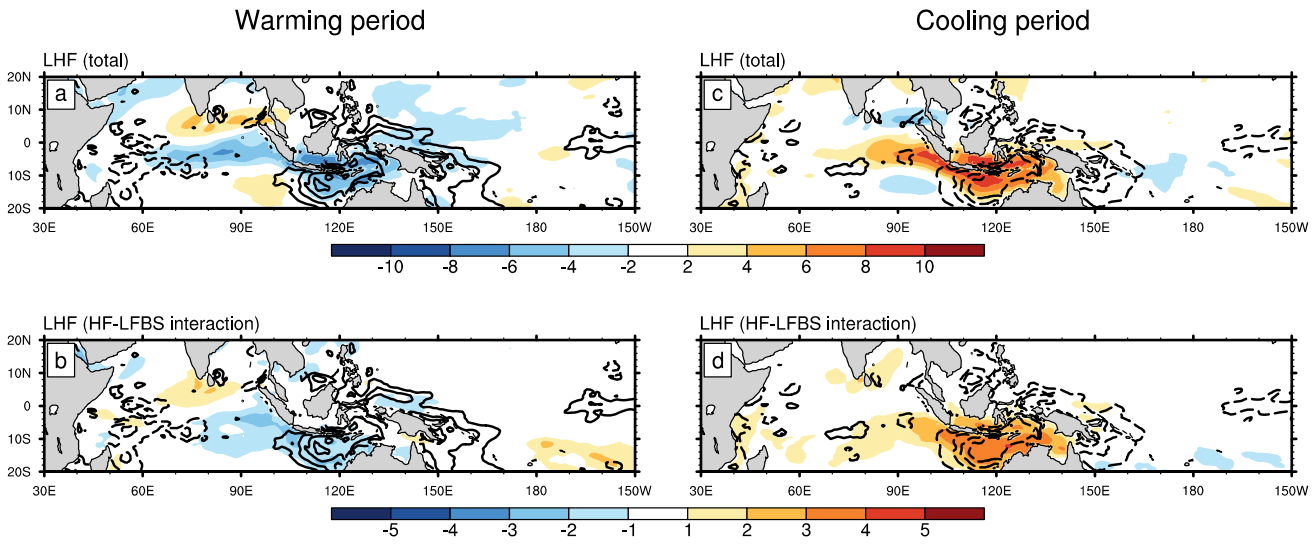


**Fig. 6** Same as Fig. 5, except that the shading represents the 20–90-day-filtered LHF calculated based on **a**, **c** the total fields and **b**, **d** HF–LFBS interaction. Units: W m$^{-2}$

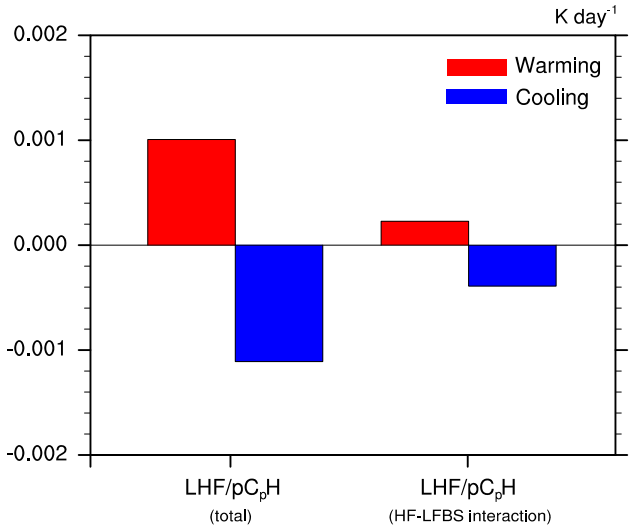


**Fig. 7** Composites of 20–90-day-filtered $LHF/\rho C_p H$ calculated based on the total fields and HF–LFBS interaction for the (red) warming and (blue) cooling periods, averaged over (90°–150° E, 15° S–0°)

(35.2%) of that from the total intraseasonal LHF to $\partial\langle T'\rangle/\partial t$ in the warming (cooling) period (Fig. 7). Therefore, high-frequency wind may be favorable for the warm (cold) SSTA ahead of (behind) the MJO convection through its maintenance of LHF and $\partial\langle T'\rangle/\partial t$.

## 4 OGCM experiments

In this section, the influence of high-frequency wind on the intraseasonal SSTA is verified by using two experiments of LICOM2.0: CTRL and EXP_noHF. First, the simulation skill of LICOM2.0 in representing surface temperature is investigated (Fig. 8). The temperature in the top layer of the ocean model (i.e., 5 m below the sea surface) is used for SST. The distribution of climatological SST from CTRL (Fig. 8a) is quite similar to that of SST from the reanalysis (Fig. 1a), showing large values in the warm pool region. The standard deviations of simulated SST and intraseasonal SSTA (Fig. 8b, c) both exhibit less variability than those

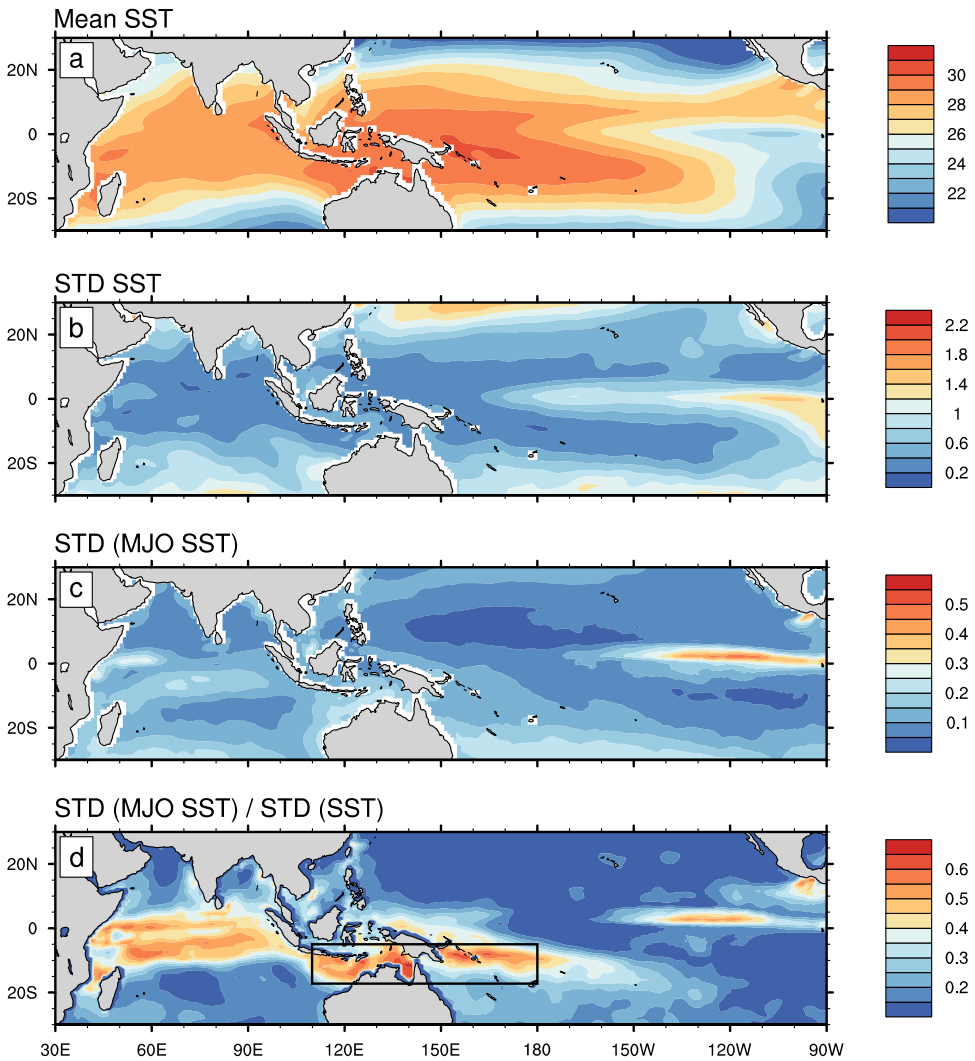


**Fig. 8** Same as Fig. 1, except for SST in CTRL. The box in **d** represents the key region (110° E–180°, 17.5° S–5° S) for model analysis

of observed SST and intraseasonal SSTA, but with a high resemblance in terms of geographic distributions (Fig. 1b, c). This may be due to the absence of air–sea coupling processes or of SST diurnal cycle in the model. In general, LICOM2.0 performs well in simulating the upper-ocean temperature. The ratio of SST variability explained by the intraseasonal SSTA (Fig. 8d) is also broadly consistent with the ratio related to observed SST (Fig. 1d), with large values over the equatorial regions from the Indian Ocean to the central Pacific. However, the maximum ratio in CTRL becomes narrower and extends more eastward into the Pacific than that in the reanalysis. Therefore, we choose (110° E–180°, 17.5° S–5° S), which shows the most significant intraseasonal SSTA variability, as the key region for model simulation analysis.

The composite of the SSTA index used to determine the evolution of 20–90-day-filtered SSTA is shown in Fig. 9. Over the key region, the local intraseasonal SSTA is getting warmer from phase − 180° to − 30° and gradually cools down after reaching the maximum at phase 0°. It is noticed that the anomalous SST also exhibits the characteristic of eastward propagation. When the coldest SSTA is located in the key region at phase − 180°, weakly warm SSTA appears in the equatorial Indian Ocean. Then, this warm SSTA strengthens and moves eastward. When it reaches the Maritime Continent, a cold SSTA initiates in the equatorial Indian Ocean. This implies that the SSTA index captures the life cycle of intraseasonal SST variation well.

Figure 10 shows the life cycles of intraseasonal SSTA, $\partial\langle T\rangle/\partial t$ and LHF from CTRL and EXP_noHF averaged over the key region. The warming effect is observed from phase − 120° to − 30° (Fig. 10a, b). As in Fig. 4, a near-quadrature phase relationship exists between the intraseasonal SSTA and $\partial\langle T\rangle/\partial t$. LHF anomaly seems to be 30°–60° behind $\partial\langle T'\rangle/\partial t$ (Fig. 10c). It is generally consistent with the reanalysis, as the maximum LHF appears slightly to the west of $\partial\langle T'\rangle/\partial t$ maximum (Fig. 6). During the warming phases (− 120° to − 30°), enhanced downward LHF is into the ocean, supporting $\partial\langle T'\rangle/\partial t$. When the high-frequency component of surface wind is removed, all of these variables become smaller. Note that the amplitude of maximum SSTA in EXP_noHF is about 9.6% smaller than that in CTRL. However, the differences between the results of CTRL and EXP_noHF for the cooling phases (30°–120°) are relatively small. This may be caused by the systematic error of LICOM2.0, as the upscale feedback in the reanalysis seems to be more important for the cooling period (35.2%) than for the warming period (22.6%; Fig. 7).

To represent the spatial differences of intraseasonal SSTA-related variability induced by the effect of high-frequency wind, Fig. 11 illustrates the horizontal distributions of intraseasonal SSTA, $\partial\langle T\rangle/\partial t$ and LHF in CTRL, EXP_noHF and their difference (EXP_noHF minus

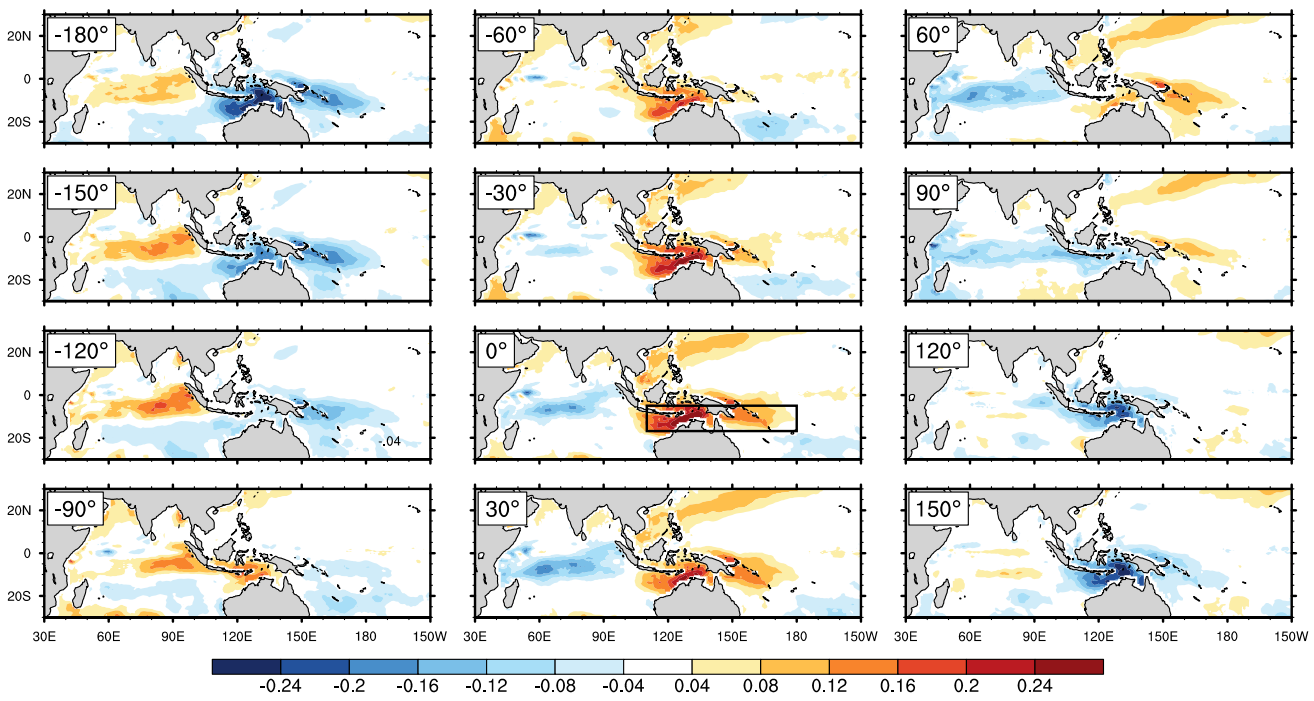


**Fig. 9** Phase evolution of 20–90-day-filtered SSTA (K). Panel in phase 0° represents the key region (110° E–180°, 17.5° S–5° S; black box) averaged intraseasonal SSTA reaching its maxima. Only the intraseasonal SSTA events with amplitude exceeding one standard deviation are chosen for phase composite

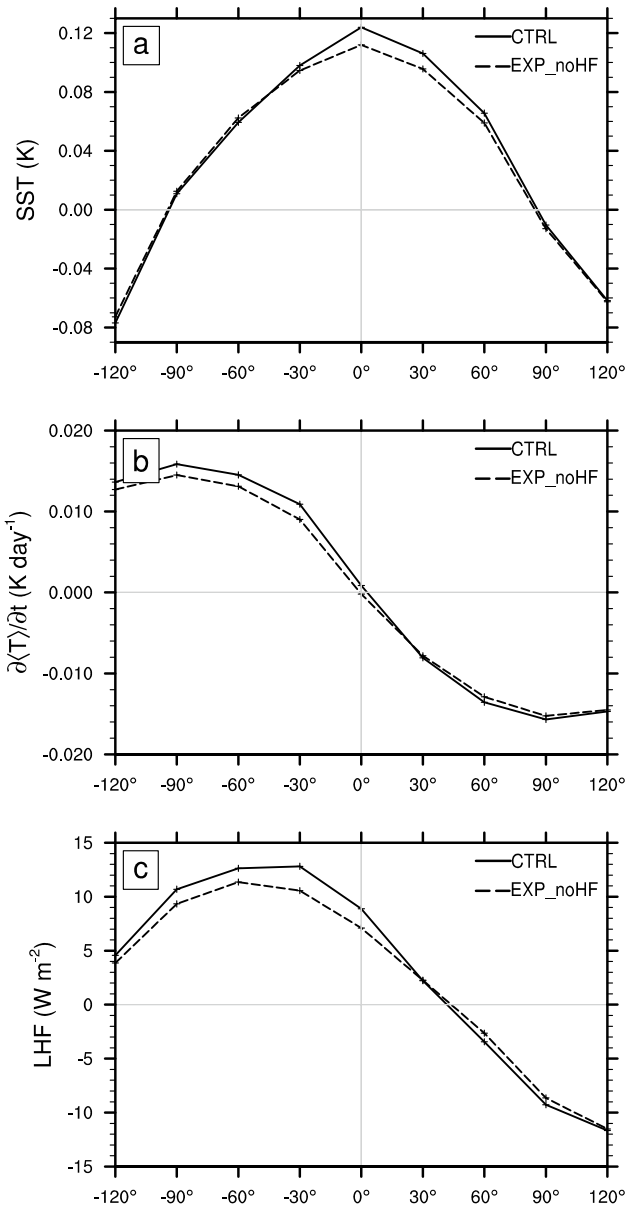


**Fig. 10** Phase evolutions of 20–90-day-filtered **a** SSTA, **b** $\partial\langle T\rangle/\partial t$ and **c** LHF in CTRL (solid line) and EXP_noHF (dashed line), averaged over (110° E–180°, 17.5° S–5° S). Downward is positive in **c**

CTRL), along with the significance test results at their peak phases (0°, − 90° and − 30° for SSTA, $\partial\langle T\rangle/\partial t$ and LHF, respectively). The patterns of intraseasonal SSTA, $\partial\langle T\rangle/\partial t$ and LHF in EXP_noHF (Fig. 11b, e, h) resemble those in CTRL (Fig. 11a, d, g), but their amplitude tends to be reduced (Fig. 11c, f, i). Focusing on the key region, we can see that large reductions of intraseasonal SSTA variability occur in the eastern Indian Ocean and western Pacific of the Southern Hemisphere, while the amplitude difference between EXP_noHF and CTRL around the Maritime Continent is quite small. The most significant changes in intraseasonal SSTA, $\partial\langle T\rangle/\partial t$ and LHF all appear in the subtropical western South Pacific with p value < 0.1 (at the 90% significance level) based on Student's *t*-test. The results were confirmed by the non-parametric Mann–Whitney test as well (not shown). The OGCM experiments results are consistent with our reanalysis data diagnosis, that is, the high-frequency wind can support the tropical intraseasonal SSTA through its contribution to LHF and $\partial\langle T'\rangle/\partial t$.

## 5 Summary and discussion

### 5.1 Summary

The impact of high-frequency wind on the intraseasonal SSTA is examined by using reanalysis data and OGCM experiments. Under the active MJO region, the total SST variability is largely explained by its intraseasonal component (> 50%), suggesting the strong forcing effect of atmosphere on the ocean. Warm SSTA always leads the MJO convection. This horizontal gradient of intraseasonal SSTA induces anomalous boundary-layer convergence, which increases atmospheric instability east of the convective center, favoring the MJO eastward propagation.

Based on the mixed-layer heat budget analysis, we calculated the contribution of each process to the SSTA. $\partial\langle T'\rangle/\partial t$ is mostly contributed by SW and decreased by LW. Both terms are strongly affected by the cloud-radiation effect of the MJO. The second contributor to $\partial\langle T'\rangle/\partial t$ is LHF, with a contribution ratio of 13.4%. Largely influenced by the MJO activity, weaker (stronger) high-frequency wind appears over the SSTA warming (cooling) region. Due to the strong nonlinearity of surface LHF, this high-frequency disturbance further upscale feedbacks to the intraseasonal LHF through the interaction with the background state. The distribution of intraseasonal LHF induced by the HF–LFBS interaction highly resembles that of the high-frequency wind and that of the total intraseasonal LHF: reduced (enhanced) LHF anomalies are observed over the positive (negative) $\partial\langle T'\rangle/\partial t$ region, supporting $\partial\langle T'\rangle/\partial t$. The high-frequency wind plays a positive role in contributing to the warm SSTA ahead of the convective center.

Two OGCM experiments using LICOM2.0 were designed to verify the effect of high-frequency wind on the intraseasonal SSTA. LICOM2.0 has a good simulation skill in representing upper-ocean temperature. Once the high-frequency wind is removed, the magnitudes of intraseasonal LHF, $\partial\langle T\rangle/\partial t$ and SSTA are all decreased. Large reductions of intraseasonal SSTA variability occur in the eastern Indian Ocean and western Pacific of the Southern Hemisphere, while amplitude difference between EXP_noHF and CTRL around the Maritime Continent is quite small. The model experiments reveal that the upscale feedback of

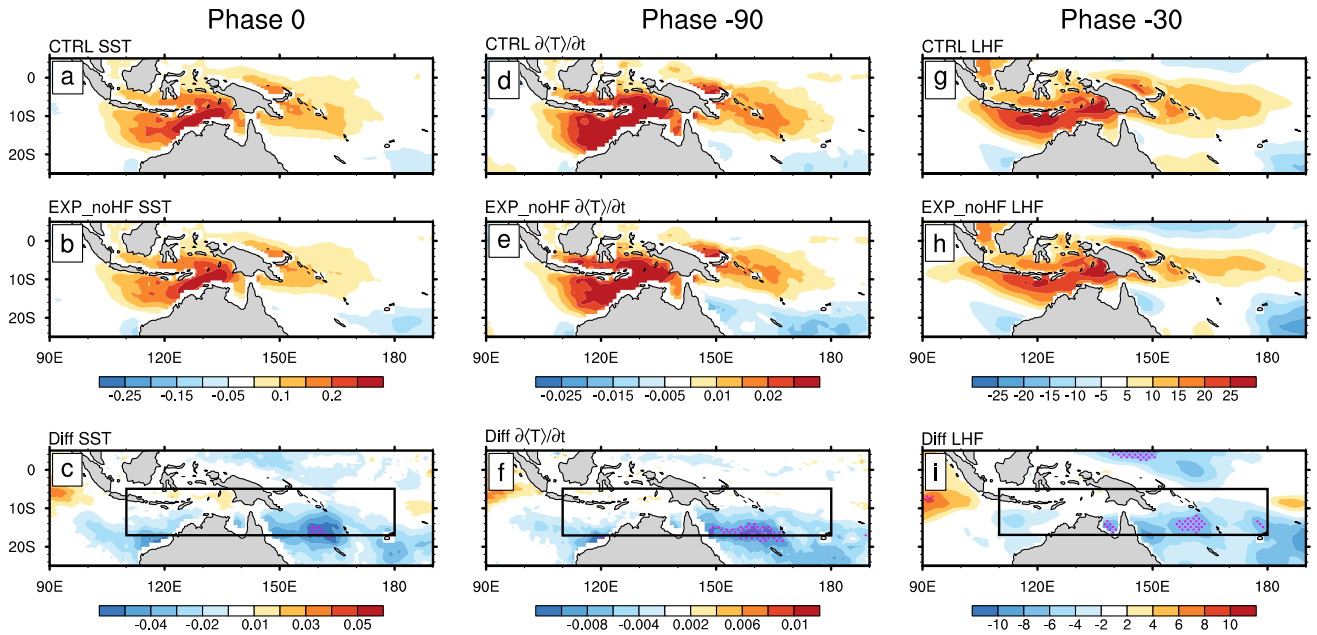


**Fig. 11** Composites of 20–90-day-filtered **a**–**c** SSTA (units: K) at phase 0°, **d**–**f** $\partial\langle T\rangle/\partial t$ (units: K day$^{-1}$) at phase −90° and **g**–**i** LHF (units: W m$^{-2}$) at phase −30° in (upper) CTRL (middle) EXP_noHF and (bottom) their difference (EXP_noHF minus CTRL). In the bottom panels, the box represents the key region (110° E–180°, 17.5°–5° S), and stippling marks the regions with statistically significant change at the 90% significance level

high-frequency wind variability accounts for 9.6% of the intraseasonal SSTA intensity. Consistent with our reanalysis data diagnosis, the high-frequency wind helps support the intraseasonal SSTA in the tropics through the maintenance of LHF and $\partial\langle T'\rangle/\partial t$. The effects of high-frequency disturbances on the intraseasonal SSTA identified by this study suggest that it is important to accurately simulate the high-frequency components for better simulating and predicting the MJO.

## 5.2 Discussion

In Gao et al. (2019), the HF–LFBS induced intraseasonal LHF is located at the MJO convective center, while the total intraseasonal LHF slightly lags behind the MJO convection. However, in this study, we found no significant phase difference between the nonlinearly rectified LHF and total intraseasonal LHF; both of them are located slightly to the west of the maximum $\partial\langle T'\rangle/\partial t$. This may be associated with the composite method used. Composites of intraseasonal OLR and LHF anomalies in Gao et al. (2019) were based on the phases of MJO convection, while the phase relationship between the intraseasonal $\partial\langle T\rangle/\partial t$ and LHF in this study is composited according to the SSTA warming and cooling periods. Compared to the time change of SSTA, surface winds are directly and strongly affected by the atmospheric convection. This may lead to a more visible phase difference between the total intraseasonal LHF and nonlinearly rectified intraseasonal LHF when the composite is based on the MJO convection.

In this study, we use daily-mean variables to diagnose the upscale feedback of high-frequency wind to the intraseasonal SSTA. Previous modeling studies have shown that diurnal forcing of shortwave radiation and surface winds can affect the diurnal cycle of SST and result further in the lower frequency variabilities of SST ranging from intraseasonal to seasonal, and even inter-annual (Bernie et al. 2005; Shinoda 2005; Guemas et al. 2011; Thushara and Vinayachandran 2014; Yang et al. 2015; Yu et al. 2017). During daytime, shortwave radiation heats the upper ocean, while during night, in the absence of insolation, surface wind tends to deepen the mixed layer and cool the ocean, via inducing vertical mixing and increasing surface turbulent fluxes.

To address the nonlinear rectification effect of diurnal variation in surface wind on the intraseasonal SSTA, we carried out additional observational diagnosis and OGCM experiments by using finer temporal resolution (6-hourly) data and compared them with the results based on the daily-mean variables. The diagnostic results based on the 6-hourly data (inclusion of diurnal cycle) indicated that the intraseasonal LHF induced by the high-frequency wind interacting with background state is of a larger amplitude than that calculated by daily-mean wind field (not shown). This suggests that the diurnal cycle of surface wind field plays a positive role in supporting the intraseasonal SSTA

variation. Our current analysis using daily-mean reanalysis data may underestimate the contribution of high-frequency wind variability to the intraseasonal SSTA variation. In contrast to the reanalysis results, the model sensitivity experiments forced by daily and 6-hourly data had trivial differences (not shown). The contribution of high-frequency wind variability to intraseasonal SSTA in the key region in the 6-hourly forcing experiments is even slightly smaller than that in the daily forcing experiments. This contrast of model results against observational results calls for in-depth study of model uncertainty in the future.

**Acknowledgements** Comments from the reviewers and Editor are deeply appreciated, which improved the quality of this paper significantly. YG and PH are supported by the National Key R&D Program of China (Grant 2018YFC1505804) and NUIST-UoR Open Project. LW is supported by the Natural Science Foundation of China (Grant 41705059). LC is supported by the Natural Science Foundation of Jiangsu Province (Grant BK20190781) and the LASG Open Project. We acknowledge the support of the Institute of Atmospheric Physics of the Chinese Academy of Sciences (IAP/CAS) for providing LICOM2.0.

## References

Ahn M-S, Kim D, Sperber KR et al (2017) MJO simulation in CMIP5 climate models: MJO skill metrics and process-oriented diagnosis. Clim Dyn 49:4023–4045. https://doi.org/10.1007/s00382-017-3558-4

Behringer D, Xue Y (2004) Evaluation of the global ocean data assimilation system at NCEP: the Pacific Ocean. In: Eighth symposium on integrated observing and assimilation systems for atmosphere, oceans, and land surface. AMS 48th annual meeting, Seattle

Bernie DJ, Woolnough SJ, Slingo JM, Guilyardi E (2005) Modeling diurnal and intraseasonal variability of the ocean mixed layer. J Clim 18:1190–1202. https://doi.org/10.1175/JCLI3319.1

Canuto VM, Howard A, Cheng Y, Dubovikov MS (2001) Ocean turbulence. Part I: one-point closure model—momentum and heat vertical diffusivities. J Phys Oceanogr 31:1413–1426. https://doi.org/10.1175/1520-0485(2001)031%3c1413:OTPIOP%3e2.0.CO;2

Canuto VM, Howard A, Cheng Y, Dubovikov MS (2002) Ocean turbulence. Part II: vertical diffusivities of momentum, heat, salt, mass, and passive scalars. J Phys Oceanogr 32:240–264. https://doi.org/10.1175/1520-0485(2002)032%3c0240:OTPIVD%3e2.0.CO;2

de Boyer Montégut C (2004) Mixed layer depth over the global ocean: an examination of profile data and a profile-based climatology. J Geophys Res 109:C12003. https://doi.org/10.1029/2004JC002378

de Szoeke SP, Edson JB, Marion JR et al (2015) The MJO and air–sea interaction in TOGA COARE and DYNAMO. J Clim 28:597–622. https://doi.org/10.1175/JCLI-D-14-00477.1

DeMott CA, Klingaman NP, Woolnough SJ (2015) Atmosphere-ocean coupled processes in the Madden-Julian oscillation. Rev Geophys 53:1099–1154. https://doi.org/10.1002/2014RG000478

DeMott CA, Benedict JJ, Klingaman NP et al (2016) Diagnosing ocean feedbacks to the MJO: SST-modulated surface fluxes and the moist static energy budget. J Geophys Res Atmos 121:8350–8373. https://doi.org/10.1002/2016JD025098

Drushka K, Sprintall J, Gille ST, Wijffels S (2012) In situ observations of Madden–Julian oscillation mixed layer dynamics in the Indian and western Pacific oceans. J Clim 25:2306–2328. https://doi.org/10.1175/JCLI-D-11-00203.1

Duvel JP, Vialard J (2007) Indo-Pacific sea surface temperature perturbations associated with intraseasonal oscillations of tropical convection. J Clim 20:3056–3082. https://doi.org/10.1175/JCLI4144.1

Duvel JP, Roca R, Vialard J (2004) Ocean mixed layer temperature variations induced by intraseasonal convective perturbations over the Indian Ocean. J Atmos Sci 61:1004–1023. https://doi.org/10.1175/1520-0469(2004)061%3c1004:OMLTVI%3e2.0.CO;2

Gao Y, Hsu P-C, Hsu H-H (2016) Assessments of surface latent heat flux associated with the Madden–Julian oscillation in reanalyses. Clim Dyn 47:1755–1774. https://doi.org/10.1007/s00382-015-2931-4

Gao Y, Hsu P-C, Li T (2019) Effects of high-frequency activity on latent heat flux of MJO. Clim Dyn 52:1471–1485. https://doi.org/10.1007/s00382-018-4208-1

Guemas V, Salas-Mélia D, Kageyama M et al (2011) Impact of the ocean mixed layer diurnal variations on the intraseasonal variability of sea surface temperatures in the Atlantic Ocean. J Clim 24:2889–2914. https://doi.org/10.1175/2010JCLI3660.1

Hendon HH, Glick J (1997) Intraseasonal air–sea interaction in the tropical Indian and Pacific oceans. J Clim 10:647–661

Hsu P-C, Li T (2012) Role of the boundary layer moisture asymmetry in causing the eastward propagation of the Madden–Julian oscillation. J Clim 25:4914–4931. https://doi.org/10.1175/JCLI-D-11-00310.1

Jin X, Zhang X, Zhou T (1999) Fundamental framework and experiments of the third generation of IAP/LASG world ocean general circulation model. Adv Atmos Sci 16:197–215. https://doi.org/10.1007/BF02973082

Klingaman NP, Woolnough SJ (2014) The role of air–sea coupling in the simulation of the Madden-Julian oscillation in the Hadley Centre model. Q J R Meteorol Soc 140:2272–2286. https://doi.org/10.1002/qj.2295

Krishnamurti TN, Oosterhof DK, Mehta AV (1988) Air–sea interaction on the time scale of 30–50 days. J Atmos Sci 45:1304–1322. https://doi.org/10.1175/1520-0469(1988)045%3c1304:AIOTTS%3e2.0.CO;2

Krishnamurti TN, Chakraborty DR, Cubukcu N et al (2003) A mechanism of the Madden–Julian oscillation based on interactions in the frequency domain. Q J R Meteorol Soc 129:2559–2590. https://doi.org/10.1256/qj.02.151

Large WG, Yeager SG (2004) Diurnal to decadal global forcing for ocean and sea-ice models: the data sets and flux climatologies. National Center for Atmospheric Research, Boulder

Lau K-M, Sui C-H (1997) Mechanisms of short-term sea surface temperature regulation: observations during TOGA COARE. J Clim 10:465–472. https://doi.org/10.1175/1520-0442(1997)010%3c0465:MOSTSS%3e2.0.CO;2

Lau K-M, Waliser DE (2012) Intraseasonal variability in the atmosphere-ocean climate system, 2nd edn. Springer, Berlin

Li T, Zhang Y, Lu E, Wang D (2002) Relative role of dynamic and thermodynamic processes in the development of the Indian Ocean dipole: an OGCM diagnosis. Geophys Res Lett 29:2110. https://doi.org/10.1029/2002GL015789

Liebmann B, Smith CA (1996) Description of a complete (interpolated) outgoing longwave radiation dataset. Bull Am Meteorol Soc 77:1275–1277

Lin P, Yu Y, Liu H (2013) Long-term stability and oceanic mean state simulated by the coupled model FGOALS-s2. Adv Atmos Sci 30:175–192. https://doi.org/10.1007/s00376-012-2042-7

Lindzen RS, Nigam S (1987) On the role of sea surface temperature gradients in forcing low-level winds and convergence in the tropics. J Atmos Sci 44:2418–2436. https://

doi.org/10.1175/1520-0469(1987)044%3c2418:OTROSS%3e2.0.CO;2
Liu H, Lin P, Yu Y, Zhang X (2012) The baseline evaluation of LASG/IAP climate system ocean model (LICOM) version 2. Acta Meteorol Sin 26:318–329. https://doi.org/10.1007/s13351-012-0305-y
Madden RA (1986) Seasonal variations of the 40–50 day oscillation in the tropics. J Atmos Sci 43:3138–3158. https://doi.org/10.1175/1520-0469(1986)043%3c3138:SVOTDO%3e2.0.CO;2
Madden RA, Julian PR (1971) Detection of a 40–50 day oscillation in the zonal wind in the tropical Pacific. J Atmos Sci 28:702–708. https://doi.org/10.1175/1520-0469(1971)028%3c0702:DOADOI%3e2.0.CO;2
Madden RA, Julian PR (1994) Observations of the 40–50-day tropical oscillation—a review. Mon Weather Rev 122:814–837. https://doi.org/10.1175/1520-0493(1994)122%3c0814:OOTDTO%3e2.0.CO;2
McPhaden MJ (2002) Mixed layer temperature balance on intraseasonal timescales in the equatorial Pacific ocean. J Clim 15:2632–2647. https://doi.org/10.1175/1520-0442(2002)015%3c2632:MLTBOI%3e2.0.CO;2
Ohlmann JC (2003) Ocean radiant heating in climate models. J Clim 16:1337–1351
Rienecker MM, Suarez MJ, Gelaro R et al (2011) MERRA: NASA's modern-era retrospective analysis for research and applications. J Clim 24:3624–3648. https://doi.org/10.1175/JCLI-D-11-00015.1
Shinoda T (2005) Impact of the diurnal cycle of solar radiation on intraseasonal SST variability in the western equatorial Pacific. J Clim 18:2628–2636. https://doi.org/10.1175/JCLI3432.1
Thushara V, Vinayachandran PN (2014) Impact of diurnal forcing on intraseasonal sea surface temperature oscillations in the Bay of Bengal. J Geophys Res Oceans 119:8221–8241. https://doi.org/10.1002/2013JC009746
Waliser DE, Graham NE (1993) Convective cloud systems and warm-pool sea surface temperatures: coupled interactions and self-regulation. J Geophys Res 98:12881. https://doi.org/10.1029/93JD00872
Wang B, Li T (1993) A simple tropical atmosphere model of relevance to short-term climate variations. J Atmos Sci 50:260–284. https://doi.org/10.1175/1520-0469(1993)050%3c0260:ASTAMO%3e2.0.CO;2
Wang L, Li T, Zhou T (2012) Intraseasonal SST variability and air–sea interaction over the Kuroshio Extension region during boreal summer. J Clim 25:1619–1634. https://doi.org/10.1175/JCLI-D-11-00109.1
Wang L, Li T, Zhou T (2015) Effect of high-frequency wind on intraseasonal SST variabilities over the mid-latitude North Pacific region during boreal summer. Clim Dyn 45:2607–2617. https://doi.org/10.1007/s00382-015-2496-2
Weare BC, Strub PT, Samuel MD (1981) Annual mean surface heat fluxes in the tropical Pacific ocean. J Phys Oceanogr 11:705–717. https://doi.org/10.1175/1520-0485(1981)011%3c0705:AMSHFI%3e2.0.CO;2
Wheeler MC, Hendon HH (2004) An all-season real-time multivariate MJO index: development of an index for monitoring and prediction. Mon Weather Rev 132:1917–1932. https://doi.org/10.1175/1520-0493(2004)132%3c1917:AARMMI%3e2.0.CO;2
Woolnough SJ, Slingo JM, Hoskins BJ (2000) The relationship between convection and sea surface temperature on intraseasonal timescales. J Clim 13:2086–2104. https://doi.org/10.1175/1520-0442(2000)013%3c2086:TRBCAS%3e2.0.CO;2
Yang Y, Li T, Li K, Yu W (2015) What controls seasonal variations of the diurnal cycle of sea surface temperature in the eastern tropical Indian Ocean? J Clim 28:8466–8485. https://doi.org/10.1175/JCLI-D-14-00826.1
Yoneyama K, Zhang C, Long CN (2013) Tracking pulses of the Madden–Julian oscillation. Bull Am Meteorol Soc 94:1871–1891. https://doi.org/10.1175/BAMS-D-12-00157.1
Yu Y, Sun D-Z (2009) Response of ENSO and the mean state of the tropical Pacific to extratropical cooling and warming: a study using the IAP coupled model. J Clim 22:5902–5917. https://doi.org/10.1175/2009jcli2902.1
Yu Y, Gao H, Shi J et al (2017) Diurnal forcing induces variations in seasonal temperature and its rectification mechanism in the eastern shelf seas of China. J Geophys Res Oceans 122:9870–9888. https://doi.org/10.1002/2017JC013473
Yuan D, Liu H (2009) Long-wave dynamics of sea level variations during Indian Ocean dipole events. J Phys Oceanogr 39:1115–1132. https://doi.org/10.1175/2008jpo3900.1
Zhang C (1996) Atmospheric intraseasonal variability at the surface in the tropical western Pacific ocean. J Atmos Sci 53:739–758. https://doi.org/10.1175/1520-0469(1996)053%3c0739:AIVATS%3e2.0.CO;2
Zhang C (2005) Madden-Julian oscillation. Rev Geophys 43:RG2003. https://doi.org/10.1029/2004RG000158
Zhang C (2013) Madden–Julian oscillation: bridging weather and climate. Bull Am Meteorol Soc 94:1849–1870. https://doi.org/10.1175/BAMS-D-12-00026.1
Zhang C, Gottschalck J (2002) SST anomalies of ENSO and the Madden–Julian oscillation in the equatorial Pacific. J Clim 15:2429–2445. https://doi.org/10.1175/1520-0442(2002)015%3c2429:SAOEAT%3e2.0.CO;2
Zhou C, Li T (2010) Upscale feedback of tropical synoptic variability to intraseasonal oscillations through the nonlinear rectification of the surface latent heat flux. J Clim 23:5738–5754. https://doi.org/10.1175/2010JCLI3468.1